Energy spectra and angular distributions of charged particles backscattered from solid targets

E S M Ali and D W O Rogers

Carleton Laboratory for Radiotherapy Physics, Ottawa Carleton Institute of Physics,
Carleton University, 1125 Colonel By Drive, Ottawa, ON K1S 5B6, Canada

E-mail: eali@physics.carleton.ca and drogers@physics.carleton.ca
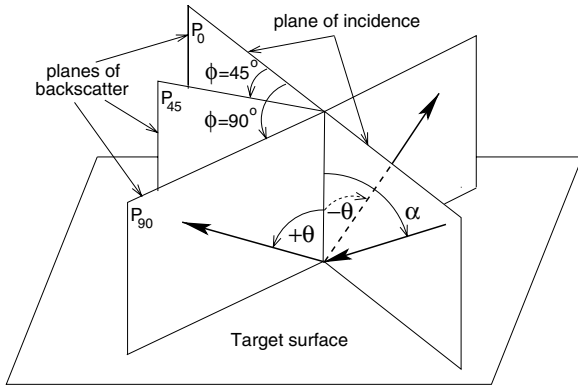
Abstract
In this study, the EGSnrc (Electron Gamma Shower) Monte Carlo radiation transport code is used to simulate the energy spectra and the angular distributions of charged particles backscattered from solid targets. The study covers the energy range 10–70 keV, which is of interest to applied physics fields such as scanning electron microscopy, microprobe analysis and x-ray imaging. Simulation results are compared with experimental data from 11 different published experiments (1954–2002). Comparisons include electrons and positrons, low- and high-Z targets, normal and oblique incidence, different backscatter angles and backscatter planes, and backscatter from thin films. EGSnrc simulation results show excellent agreement with the majority of the published experimental data. Possible experimental and computational uncertainties explaining the few noted discrepancies are discussed. This study concludes that EGSnrc produces accurate backscatter data in the kilovoltage energy range. A documented EGSnrc user-code customized for backscatter calculations is available from the authors at http://www.physics.carleton.ca/clrp/backscatter.

(Some figures in this article are in colour only in the electronic version)

1. Introduction

Accurate knowledge of the energy spectra and angular distributions of kilovoltage charged particles (electrons and positrons) backscattered from solid targets is important to many applied physics fields. In the field of analytical surface science, this knowledge is used in studying image contrast in scanning electron microscopy [1], developing correction factors for quantitative electron probe microanalysis [2, 3], evaluating layered structures and surface defects in surface spectroscopy [4], diffraction studies [5] and thin-film applications [6]. In the field of medical physics, this knowledge is used in predicting dose perturbations due to high-Z inhomogeneities in tissue [7], studying the performance of x-ray tubes when placed in the magnetic field of a magnetic resonance scanner [8,9] and quantifying the effect of off-focal radiation on the output of x-ray systems [10]. From an academic perspective, this knowledge helps in understanding the processes involved in charged particle backscatter, and in evaluating the merits of various theories available to explain them. Over the years, there have been a number of Monte Carlo studies of the energy spectra and the angular distributions of backscattered charged particles in the kilovoltage energy range [3, 11–19]. However, there are many simplifying approximations in the models used, and these in-house Monte Carlo codes are not usually available to the researchers of the applied physics community with appropriate manuals and source-code documentation. In addition, a few investigators did not present comparisons of their Monte Carlo simulation results with experimental data. An alternative approach is to perform backscatter calculations using the currently available general-purpose Monte Carlo codes such as PENELOPE [20, 21], ETRAN-based [22] codes (i.e. MCNP [23] and ITS [24]), GEANT4 [25] or EGSnrc [26, 27]. The EGSnrc (Electron Gamma Shower) Monte Carlo code has sophisticated low-energy physics comparable to those in PENELOPE;

Figure 1. Definition of angles and planes used in this study.

however, PENELOPE is considerably slower [28] and requires careful tuning of its simulations parameters [29], unlike EGSnrc.

   This study tests the capability of EGSnrc to predict the energy spectra and the angular distributions of backscattered charged particles. In a related study [30] (called paper I henceforth), EGSnrc is shown to predict charged particle backscatter coefficients within ∼4% of the average of the majority of published experimental data, which is considered excellent given the scatter in the experimental data and the large uncertainties associated with them. In our current study, a new EGSnrc user-code, dedicated to backscatter calculations, is developed. Simulation results are compared with experimental data from 11 different published experiments. The comparisons cover the energy range 10–70 keV and include electrons and positrons, low- and high-Z targets, normal and oblique incidence, different backscatter angles and backscatter planes and backscatter from thin films.

2. Definitions

There is a large variation between different investigators in their definition of the parameters used to characterize the backscatter of charged particles. Because this study compares data from more than one experiment on the same graph, consistent terminology is needed. Figure 1 and the remainder of this section define the parameters used throughout this study. E_0 (in keV) is the kinetic energy of the incident monoenergetic charged particle beam. E (in keV) is the kinetic energy of the backscattered charged particle. Z is the atomic number of the target material. The incidence angle, α (in degrees, $0 \leqslant \alpha < 90°$), is the angle between the vector of the incident beam and the vector normal to the target surface; the two vectors define the plane of incidence, P_0. The backscatter angle, θ (in degrees, $-90° < \theta < 90°$), is the angle between the vector of the backscattered charged particle and the vector normal to the target surface; the two vectors define the plane of backscatter, P_ϕ, where ϕ (in degrees, $0 \leqslant \phi \leqslant 90°$) is the angle between the plane of backscatter and the plane of incidence. For this study, three backscatter planes (P_0, P_{45} and P_{90}) are investigated. The backscatter angle θ is positive in the forward half of P_ϕ and negative in the backward half. $\Delta\Omega$ (in sr, $0 < \Delta\Omega \leqslant 2\pi$) is the solid angle subtended by the detector. If
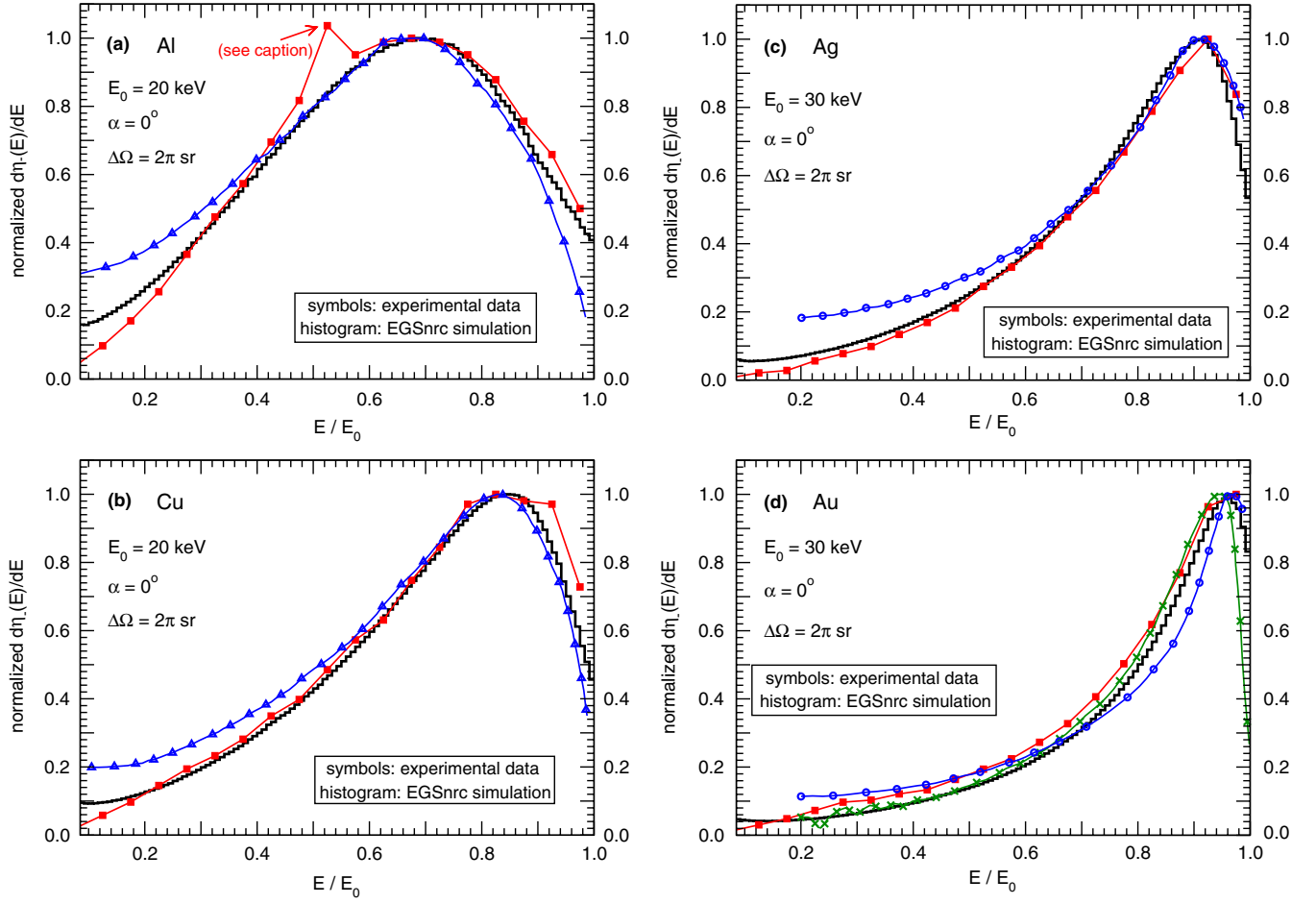
the detector is a hemispherical collector then $\Delta\Omega = 2\pi$ sr. The charged particle backscatter coefficient, η (in %), is the number of charged particles that backscatter into the hemisphere above the target surface divided by the number of incident particles. By definition, η does *not* include electrons from secondary electron emission which is the generation of very low-energy surface electrons (conventionally with kinetic energy <50 eV). The backscatter coefficients for electrons and positrons are η_- and η_+, respectively. For energy spectra, to differentiate between the spectra measured by a small detector at a fixed point in space and those measured by a hemispherical collector, the terms 'local' and 'overall' are used, respectively. The local energy spectrum, $\mathrm{d}^2\eta(P_\phi, E, \theta)/\mathrm{d}E\,\mathrm{d}\Omega$ (in keV^{-1} sr^{-1}), is the number of charged particles backscattered in a given plane, P_ϕ, with energy between E and $E + \mathrm{d}E$, at a backscatter angle between θ and $\theta + \mathrm{d}\theta$, per unit energy, per unit solid angle. The overall energy spectrum, $\mathrm{d}\eta(E)/\mathrm{d}E$ (in keV^{-1}), is the number of charged particles backscattered in the hemisphere above the target surface, with energy between E and $E + \mathrm{d}E$, per unit energy. Finally, the angular distribution, $\mathrm{d}\eta(P_\phi, \theta)/\mathrm{d}\Omega$ (in sr^{-1}), is the number of charged particles backscattered in a given plane, P_ϕ, at a backscatter angle between θ and $\theta + \mathrm{d}\theta$, per unit solid angle. These definitions should be used to interpret the graphs in section 4.

3. Methods

3.1. Experimental measurements

This study includes experimental data from 11 different published experiments reported between 1954 and 2002 [16, 17, 31–39]. Most of the experimental data were digitized electronically from their original sources because they are not available in tabular form. The only mathematical manipulations performed on the experimental data are standard conversions of angles, bins, units and coordinate systems. Examples of such manipulations are the conversion of the integral energy spectra in Darlington [32] into their differential equivalent, and the conversion of the polar data in Darlinski [33] into their Cartesian equivalent. Additional notes on specific experiments are mentioned in section 4.

   Measurements of charged particle backscatter characteristics are not trivial, and they are fraught with many sources of uncertainty. In paper I, a description of typical backscatter experiments and the uncertainties associated with the measurements of η_- and η_+ are discussed. The reasons for these uncertainties include secondary electron emission (defined in section 2), grid correction factors, voltage bias effects, surface contamination, setup and operational constraints and fluctuations, alignment issues, incident beam masking, detector entrance window, detector masking, etc—see paper I for a more complete discussion. Most of these uncertainties affect the measurements of energy spectra and angular distributions as well. In addition, the following uncertainties are specific to the current study. Small incident beam movements can cause fluctuations in the energy response of the detector [12]. Converting the recorded energy fluence spectrum, i.e. $E\,\mathrm{d}\eta(E)/\mathrm{d}E$, into a fluence spectrum, i.e. $\mathrm{d}\eta(E)/\mathrm{d}E$, causes the lower portion
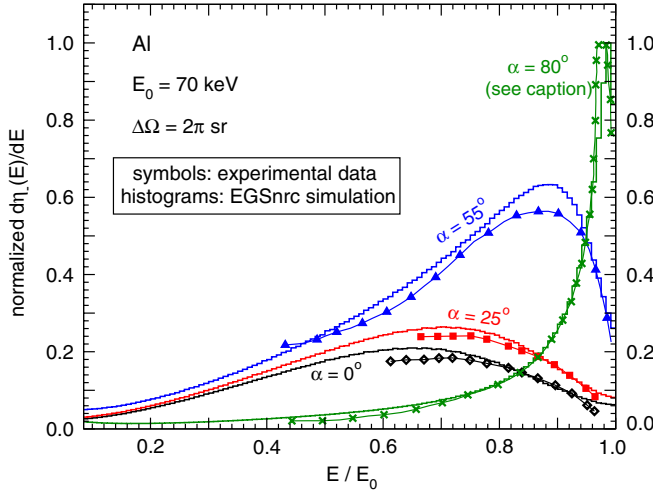
Figure 2. Overall energy spectra of electrons backscattered from semi-infinite targets of aluminium, copper, silver and gold for normal incidence. See section 2 for definitions of the parameters used. Experimental data are from [32] (■), [34] (×), [38] (○) and [39] (△). Data below $E/E_0 \sim 0.1$ are either unavailable or too noisy. In panel a, the anomalous point labelled with an arrow could be a typo in table 3 from Darlington [32], or it could be due to experimental instabilities in the energy recorder.

of the spectrum to have poorer resolution [31, 40]. Detector pulse pileup can distort the true energy spectrum if not carefully accounted for [16]. Deconvolving the true energy spectrum from the detector response always has varying degrees of uncertainty associated with it [16, 41]. Detector energy calibration and the exact point of zero energy loss can cause energy shifts in the recorded energy spectrum [31, 40]. The exact positioning of the detector in high gradient regions affects the accuracy of the angular distribution measurements, introducing uncertainties up to 12% for extreme angular distribution gradients [33]. The reader is referred to the original articles of the experiments for a more complete description of the experiments and their associated uncertainties.
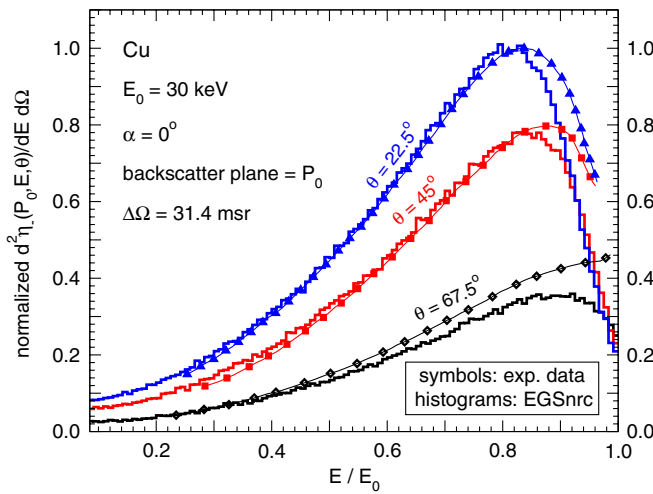
3.2. Monte Carlo simulations

This study uses the EGSnrc Monte Carlo code [26, 27] for the simulations. The code has been in development—through its predecessors—for the past three decades, and it is currently the most heavily used Monte Carlo code in medical physics. EGSnrc provides accurate and artefact-free simulation of electron, positron and photon transport in all media, both in the kilovoltage and megavoltage range. The EGSnrc *user-codes* can simulate various geometry configurations commonly

encountered in applied physics fields. In addition, there is a C++ interface that supports general geometry, scoring and source routines [42]. EGSnrc offers accurate low-energy physics for photons and for charged particles with kinetic energy ⩾ 1 keV. For photons, in addition to the standard photon physics, the code includes accurate coherent scattering form factors, binding effects in Compton scattering, photoelectron angular sampling, and accurate relaxation cascades after the creation of atomic vacancies (including Auger and Coster–Kronig electrons). For charged particles, the code uses the condensed history technique, which speeds up the calculations by many orders of magnitude while agreeing within 0.1% with single scattering calculations [26]. Other charged particle physics in EGSnrc include: explicit account of the differences in the stopping powers between positrons and electrons [43], electron impact ionization [44] whereby electrons directly create vacancies in the inner atomic shells, spin effects in electron elastic scattering, improved bremsstrahlung angular sampling, comprehensive treatment of inelastic collisions and inclusion of the density effect to take into account the polarization of the medium by the passing charged particle. For cross-section data, EGSnrc uses the most accurate data available for photons and charged particles [45–47]. For
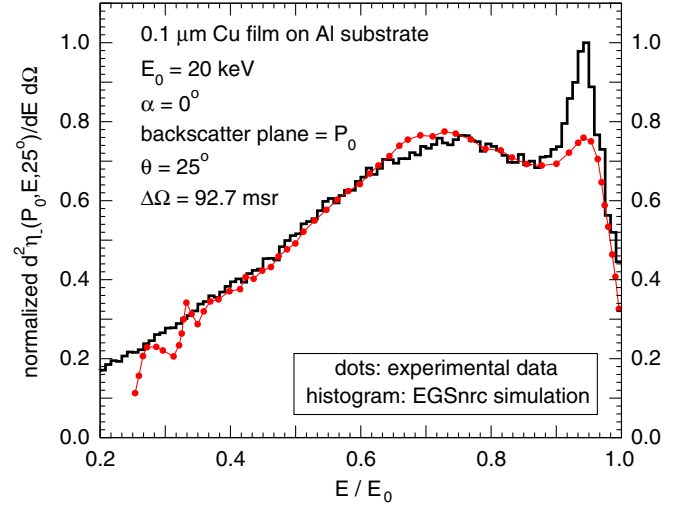
Figure 3. Variation of the overall energy spectra of backscattered electrons with the angle of incidence (α) for 70 keV electrons incident on aluminium. Experimental data are from [35]. For $\alpha = 80°$, both experimental data and EGSnrc simulation results are scaled down by a factor of five for clarity of the other curves. For $\alpha = 0°$, it was hard to accurately digitize the experimental curve due to poor resolution.

Figure 5. Local energy spectrum of 20 keV electrons backscattered from a thin copper film on an aluminium substrate. Experimental data are from [17]. Experimental data start at $E/E_0 = 0.25$, and they are noisy up to $E/E_0 \sim 0.375$. Normalization is arbitrary (i.e. not largest-peak to largest-peak).
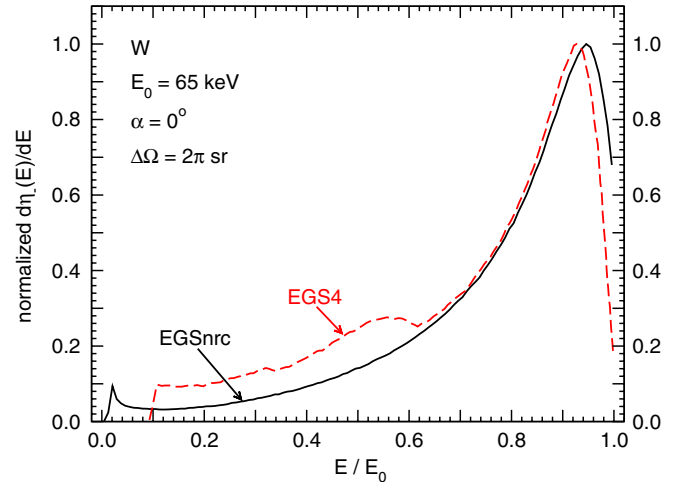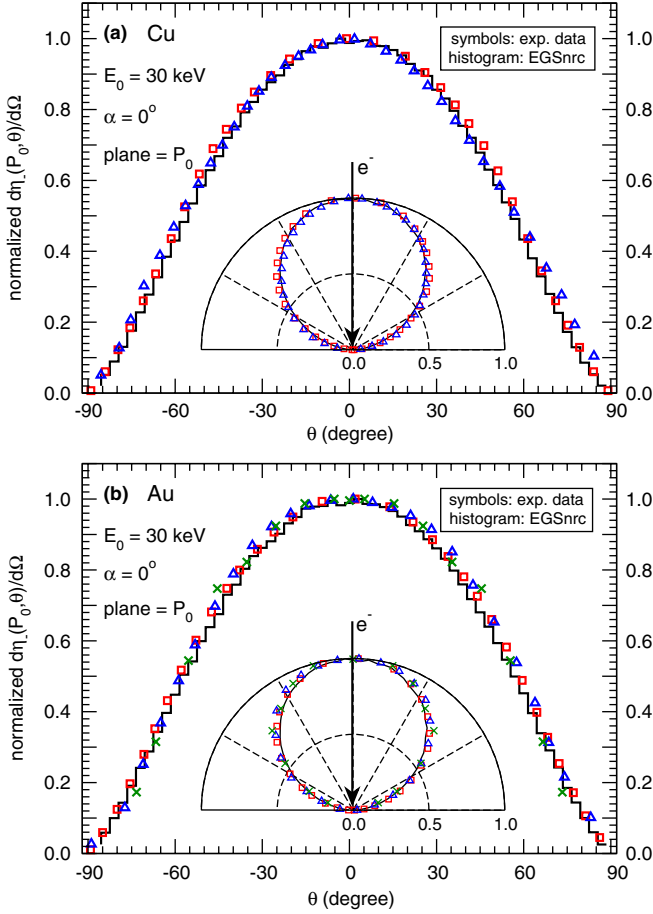

Figure 4. Variation of the local energy spectra of backscattered electrons with the backscattering angle (θ) for 30 keV electrons normally incident on copper. Experimental data are from [31].

Figure 6. Comparison between simulation results using EGSnrc (our study) and EGS4 [9] for the overall energy spectrum of 65 keV electrons backscattered from a semi-infinite tungsten target.

more details on the code, the reader is referred to the EGSnrc manual [27] and the references therein.

As part of this study, a new EGSnrc user-code, dedicated to backscatter calculations, is developed. The inputs to the user-code are: the target specifications, the type, energy and angle of the incident charged particle beam, the cut-off energies for photons and charged particles below which their transport is terminated and their energy is deposited locally, the backscatter planes of interest (through the angle ϕ), the detector locations of interest (a hemispherical detector with $\Delta\Omega = 2\pi$ sr is possible), the solid angle subtended by each detector, and the desired bin widths for the output histograms. The output of the user-code is the charged particle backscatter coefficient, the energy spectra at the detector locations specified by the user, and the angular distributions in the backscatter planes specified

by the user. In this study, a typical simulation includes a pencil beam of monoenergetic charged particles ($10 \leqslant E_0 \leqslant 70$ keV) incident on a sample with thickness larger than the range of the charged particles in the sample material, except when thin-film targets are simulated. Three backscatter planes are investigated (P_0, P_{45} and P_{90}) to compare with available experimental data. Our sensitivity analysis shows that both energy spectra and angular distributions are sensitive to the choice of $\Delta\Omega$, with the latter being more sensitive. For this reason, $\Delta\Omega$ is varied between simulations to match the specific experiment being simulated, and its value is reported in all graphs in section 4. The bin widths chosen for the energy spectra and angular distributions are ($E_0/120$) keV and $3°$, respectively. Charged particles and photons are tracked down to a kinetic energy of 1 keV which introduces $\leqslant 3\%$ systematic uncertainty in EGSnrc results—see paper I for a full discussion. All simulations are analogue, i.e. no variance reduction techniques
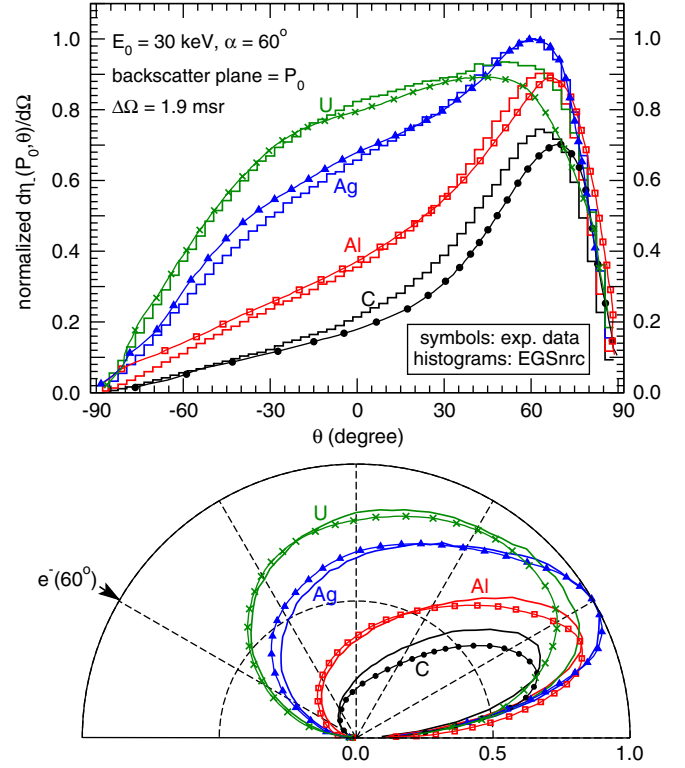
Figure 7. Angular distribution of 30 keV electrons backscattered from semi-infinite targets of copper and gold. See section 2 for definition of the parameters used. Experimental data are from [31] (□), [33] (△) and [34] (×). $\Delta\Omega = 31.4, 1.9, 0.9$ and 3.2 msr for the three experiments and for the EGSnrc simulation, respectively. Results are presented in Cartesian and polar forms.

are employed. Using a single 3.0 GHz Intel® Woodcrest 64-bit processor, the CPU time needed to reach an average uncertainty of ~1% on the output profiles ranges from a few minutes for overall energy spectra and for angular distributions using relatively large detectors, to a few tens of hours for local energy spectra using very small detectors with high-energy incident charged particles.

4. Results and discussion

In this section, comparisons are presented between EGSnrc simulation results and experimental data for the energy spectra and angular distributions of backscattered charged particles. In any given figure, the highest peak in the EGSnrc results and the highest peak in the experimental data are both normalized to unity unless otherwise stated. Other data in the figure are normalized by the same factor to preserve the relative shapes and areas under different curves. No error bars are shown on the experimental data because in most experiments only the overall uncertainties are discussed without providing individual error bars. Experimental uncertainties of ~10% are not uncommon. For the EGSnrc histograms, as discussed

Figure 8. Variation of the angular distribution of backscattered electrons with the target material at oblique incidence for 30 keV incident electrons. Experimental data are from [33].
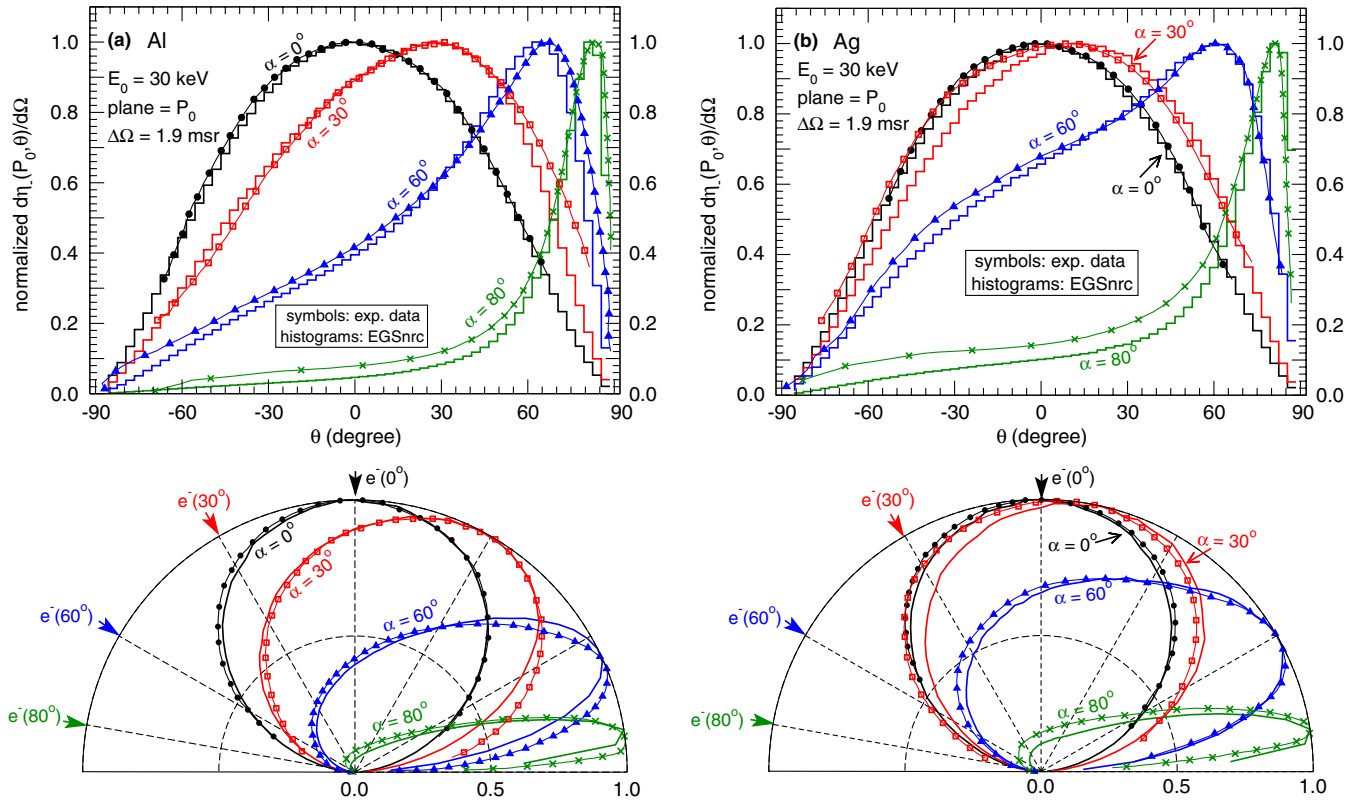
in section 3.2, the systematic and statistical uncertainties are estimated to be ⩽3% and ~1%, respectively, and they are not shown for clarity of the graphs.

4.1. Energy spectra

Figure 2 shows the overall energy spectra of electrons backscattered from semi-infinite targets of aluminium, copper, silver and gold for normal incidence. As Z increases, the spectra peak closer to the original incident energy because backscattered electrons undergo more large angle elastic scattering deflections. The slight energy shift among the spectra from different experiments (more noticeable at the peaks) could be due to energy calibration uncertainties in the experiments. There are large variations among different experiments in the lower portions of the spectra, exceeding the uncertainties reported by investigators, e.g. ~10% in Bishop [31]. These differences are mainly due to the limited detector resolution in that energy range [31]. Given the variations between experiments, it can be said that the spectra generated by EGSnrc are well within the average of the experimental measurements.

Figure 3 shows the variation of the overall energy spectrum of backscattered electrons with the angle of incidence (α) for 70 keV electrons incident on aluminium. As α increases, the electrons penetrate less and lose less energy. This is demonstrated by the broad spectrum at $\alpha = 0°$, which gets narrower and peaks towards higher energies as α increases. The area under the curves also increases with α because the portion of the differential elastic scattering distribution that

Figure 9. Variation of the angular distribution of backscattered electrons with the angle of incidence (α) for 30 keV electrons incident on aluminium and silver. All experimental data are normalized to unity at their peak because they are from multiple graphs in [33] with no common normalization.

falls in the backscatter hemisphere increases with α, and thus more electrons backscatter out of the sample. The figure shows that EGSnrc simulation results reproduce the experimental measurements well.

Figure 4 shows the variation of the local energy spectrum of backscattered electrons with the backscatter angle (θ) for 30 keV electrons normally incident on copper. As mentioned above, the energy shift between the experimental data and the EGSnrc simulation results could be due to energy calibration uncertainties in the experiment because the good agreement in figures 2 and 3 suggest that the energy peaks calculated using EGSnrc are correct. The discrepancy at $\theta = 67.5°$ could be partially due to the increased experimental uncertainties as near-grazing incidence is approached, e.g. detector masking, surface contamination, etc—see paper I, and partially due to the increased importance of electron diffraction (i.e. collective wave-like elastic scattering of electrons by the atoms of a crystalline array) at near-grazing incidence which is not modelled in EGSnrc. Overall, EGSnrc simulation results in figure 4 reproduce the experimental measurements reasonably well. In separate comparisons of the mean and most probable energies of the spectra of backscattered electrons (not shown), the EGSnrc-calculated values for 30 keV electrons normally incident on aluminium, copper, silver and gold are found to be within 5% of those from four different experiments [31, 32, 37, 38] which is well within the uncertainties of the experimental data discussed above.

For backscatter from thin films, figure 5 shows the local energy spectrum of electrons backscattered at $\theta = 25°$ in

plane P_0 from a 0.1 μm copper film (equivalent to 6% of the CSDA range of 20 keV electrons in copper) deposited on an aluminium substrate. EGSnrc reproduces the features of the energy spectrum very well, except for the magnitude of the high-energy peak which is produced by the copper thin film. Rau *et al* [17], who measured the spectrum in figure 5, showed the same over-estimate of the high-energy peak in their Monte Carlo simulation. This discrepancy could be partially due to experimental uncertainties in the film thickness and partially due to the lack of energy loss straggling in the Monte Carlo simulations.

Before closing the discussion on energy spectra, it is worth noting the difference between EGSnrc and its predecessor EGS4 [48] in evaluating these spectra. A recent study [9] used EGS4 to generate the energy spectrum of backscattered electrons when 65 keV monoenergetic electrons normally impinge onto a semi-infinite tungsten target. Figure 6 shows a comparison between the spectrum calculated using EGS4 [9] and our EGSnrc-calculated spectrum. In addition to the slight energy shift, the features exhibited by the spectrum calculated using EGS4 are not observed in any of the experimental data presented above.
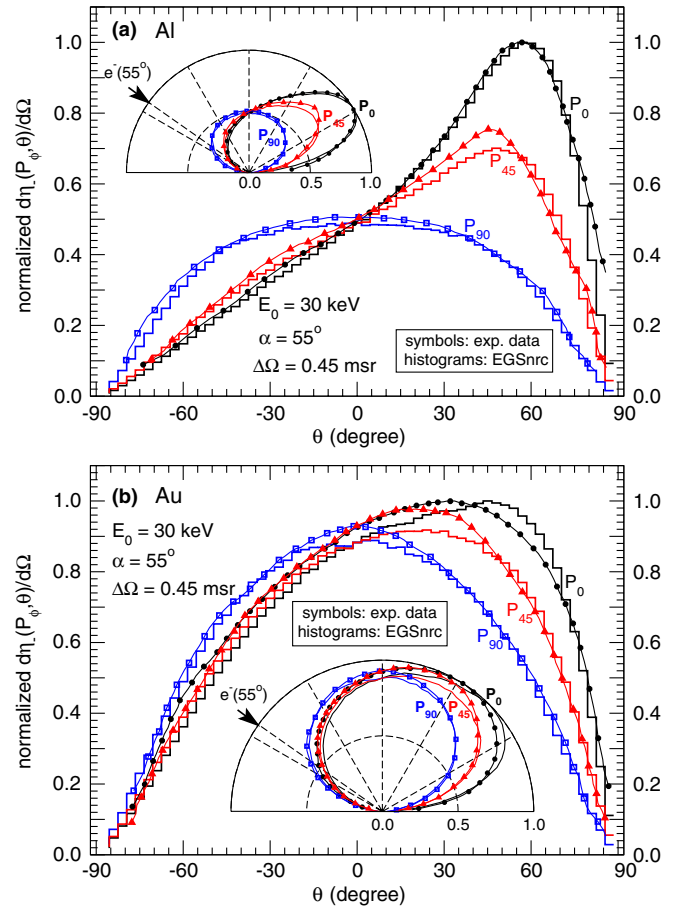
4.2. Angular distributions

Figure 7 shows the angular distribution in plane P_0 for normally incident electrons after they backscatter from semi-infinite targets of copper and gold. For normal incidence, the angular distribution exhibits a cosine-like distribution,

i.e. $d\eta_-(P_\phi, \theta)/d\Omega$ is almost directly proportional to $\cos\theta$, which shows as a circle in the polar plots. At large θ (close to $90°$ and $-90°$), the angular distribution deviates slightly from a perfect cosine. Also for normal incidence, the angular distribution does not vary much with Z (the profiles for copper and gold are almost the same). The figure shows that for both medium- and high-Z targets, EGSnrc simulation results reproduce the experimental data very well. Figure 8 shows the variation of the angular distribution with the atomic number of the target material (Z) for oblique incidence. Unlike the normal incidence case, the angular distribution at oblique incidence varies dramatically with Z. There are discrepancies between the EGSnrc simulation results and experimental data for carbon and uranium. A normalization scheme other than the one adopted in this study could improve the agreement for those elements but worsen it for others. Figure 9 shows the variation of the angular distribution with the angle of incidence (α) for 30 keV electrons incident on aluminium and silver. The number of backscattered electrons per unit solid angle peaks near the 'reflection' or the 'mirror' angle of α, which becomes more obvious as α increases. EGSnrc simulation results reproduce the experimental data very well, except for silver at $\alpha = 30°$ in the backward portion of the distribution. The discrepancy at $\alpha = 80°$ for both aluminium and silver can be attributed to the experimental and computational uncertainties associated with near-grazing incidence as discussed for figure 4 above. Figure 10 shows the variation of the angular distribution with the plane of backscatter (P_ϕ) for oblique incidence ($\alpha = 55°$) of 30 keV electrons on aluminium and gold. For aluminium, the angular distribution in plane P_0 peaks at the 'mirror' angle of α. As P_0 rotates $45°$ to become P_{45}, the angular distribution gets broader. As P_{45} rotates another $45°$ to become P_{90} (perpendicular to P_0), the angular distribution becomes symmetric around $\theta = 0°$ as expected due to symmetry. In the polar plots, as the plane of backscatter rotates from P_0 to P_{90}, the cigar-like angular distribution gradually changes to a pancake-like one. The figure shows that EGSnrc simulation results reproduce the experimental data well, with the agreement being better for aluminium than it is for gold.

Figure 11 shows the angular distributions of 10 and 15 keV electrons backscattered in plane P_0 from a composite thin film made of 20 nm of gold followed by 20 nm of aluminium oxide (Al_2O_3). At such low energies, the disagreement could partially be due to the limitations of the underlying theoretical models used in EGSnrc—see paper I for a full discussion. Because only one experiment is available and with a very limited number of data points, it can only be concluded that EGSnrc qualitatively reproduces angular distributions of backscattered electrons from composite thin films.

Figure 12 shows the variation of the angular distribution with the angle of incidence (α) for 35 keV positrons incident on aluminium and gold targets. The profiles resemble those of backscattered electrons, and arguments similar to those made for electrons can also be made for positrons. As with electrons, EGSnrc reproduces the experimental data very well.
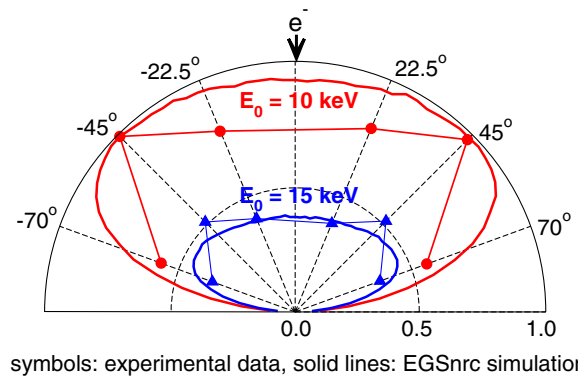

Figure 10. Variation of the angular distribution of backscattered electrons with the plane of backscatter (P_ϕ) for oblique incidence of 30 keV electrons on aluminium and gold. Experimental data are from [35].

Figure 11. Angular distribution of electrons backscattered from a composite thin film for $E_0 = 10$ (●) and 15 keV (▲). Experimental data are from [36]. Only six experimental data points are available at each energy, and they are joined by a thin line for clarity.

5. Conclusions

This study used the EGSnrc Monte Carlo radiation transport code to simulate the energy spectra and the angular

Figure 12. Variation of the angular distribution of backscattered positrons with the angle of incidence (α) for 35 keV positrons incident on aluminium and gold targets. Experimental data are from [16]. The number of experimental data points reported in [16] is limited.

distributions of charged particles backscattered from solid targets in the kilovoltage energy range. Comparisons with experimental data show excellent agreement in most cases. The noted discrepancies are most likely due to systematic experimental uncertainties as indicated by the fluctuations between different experiments measuring the same profiles. For energies $\sim$10 keV and below, the discrepancies can partially be attributed to the limitations of the underlying theoretical models used in EGSnrc. Overall, EGSnrc can be used to generate accurate catalogues of kilovoltage backscatter data, which are needed in many applied physics fields. A documented EGSnrc user-code customized for backscatter calculations is available from the authors at http://www.physics.carleton.ca/clrp/backscatter.

Acknowledgments

References

[1] Spranck M, Kässens M and Reimer L 1995 Influence of the angular distribution of backscattered electrons on signals at different take-off angles in low-voltage scanning electron microscopy (LVSEM) *Scanning* **17** 97–105

[2] Love G and Scott V D 1978 Evaluation of a new correction procedure for quantitative electron probe microanalysis *J. Phys. D: Appl. Phys.* **11** 1369–76

[3] Merlet C 1992 Accurate description of surface ionization in electron probe microanalysis: an improved formulation *X-Ray Spectrom.* **21** 229–38

[4] Schultz P J and Lynn K G 1988 Interaction of positron beams with surfaces, thin films and interfaces *Rev. Mod. Phys.* **60** 701–79

[5] Chambers S A, Chen H W, Vitomirov I M, Anderson S B and Weaver J H 1986 Direct observation of elastic strain and relaxation at a metal–metal interface by Auger electron diffraction: Cu/Ni(0 0 1) *Phys. Rev.* B **33** 8810–13

[6] Niedrig H 1982 Electron backscattering from thin films *J. Appl. Phys.* **53** R15–R49

[7] Buffa F A and Verhaegen F 2004 Backscatter and dose perturbations for low- to medium-energy electron point sources at the interface between materials with different atomic numbers *Radiat. Res.* **162** 693–701

[8] Wen Z, Fahrig R, Conolly S and Pelc N J 2007 Investigation of electron trajectories of an x-ray tube in magnetic fields of MR scanners *Med. Phys.* **34** 2048–58

[9] Wen Z, Pelc N J, Nelson W R and Fahrig R 2007 Study of increased radiation when an x-ray tube is placed in a strong magnetic field *Med. Phys.* **34** 408–18

[10] Ali E S M and Rogers D W O 2008 Quantifying the effect of off-focal (extra-focal) radiation on the output of x-ray systems *Med. Phys.* submitted

[11] Bishop H E 1967 Electron scattering in thick targets *Br. J. Appl. Phys.* **18** 703–15

[12] Coleman P G, Albrecht L, Jensen K O and Walker A B 1992 Positron backscattering from elemental solids *J. Phys.: Condens. Matter* **4** 10311–22

[13] Dapor M 1992 Monte Carlo simulation of backscattered electrons and energy from thick targets and surface films *Phys. Rev.* B **46** 618–25

[14] Kuhr J C and Fitting H J 1999 Monte Carlo simulation of electron emission from solids *J. Electron Spectrosc.* **105** 257–73

[15] Massoumi G R, Hozhabri N, Jensen K O, Lennard W N, Lorenzo M S and Schultz P J 1992 Positron and electron backscattering from solids *Phys. Rev. Lett.* **68** 3873–6

[16] Massoumi G R, Lennard W N and Schultz P J 1993 Electron and positron backscattering in the medium-energy range *Phys. Rev.* B **47** 11007–18

[17] Rau E, Hoffmeister H, Sennov R and Kohl H 2002 Comparison of experimental and Monte Carlo simulated BSE spectra of multilayered structures and 'in-depth' measurements in a SEM *J. Phys. D: Appl. Phys.* **35** 1433–7

[18] Valkealahti S and Nieminen R M 1984 Monte Carlo calculations of keV electron and positron slowing down in solids II *Appl. Phys.* A **35** 51–9

[19] Ze-jun D and Ziqin W 1993 A comparison of Monte Carlo simulations of electron scattering and x-ray production in solids *J. Phys. D: Appl. Phys.* **26** 507–16

[20] Baro J, Sempau J, Fernandez-Varea J M and Salvat F 1995 PENELOPE: an algorithm for Monte Carlo simulation of the penetration and energy loss of electrons and positrons in matter *Nucl. Instrum. Methods* B **100** 31–46

[21] Salvat F, Fernandez-Varea J M, Baro J and Sempau J 2003 PENELOPE, a code system for Monte Carlo simulation of electron and photon transport *University of Barcelona Report*

[22] Berger M and Seltzer S 1973 ETRAN Monte Carlo code system for electron and photon transport through extended media *Report* CCC-107, Radiation Shielding Information Centre, Oak Ridge National Laboratory (ORNL), Oak Ridge, TN

[23] Brown F B (ed) 2003 MCNP—A general Monte Carlo N-particle transport code Version 5 *Report* LA-UR-03-1987, Los Alamos National Laboratory, Los Alamos, NM

[24] Halbleib J A and Mehlhorn T A 1984 ITS: the integrated TIGER series of coupled electron/photon Monte Carlo transport codes *Sandia Report* SAND84-0573

[25] Agostinelli S *et al* 2003 GEANT4—a simulation toolkit *Nucl. Instrum. Methods* A **506** 250–303

[26] Kawrakow I 2000 Accurate condensed history Monte Carlo simulation of electron transport: I. EGSnrc, the new EGS4 version *Med. Phys.* **27** 485–98

[27] Kawrakow I and Rogers D W O 2007 The EGSnrc Code System: Monte Carlo simulation of electron and photon transport *NRC Technical Report* PIRS-701 v4-2-2-5, National Research Council of Canada, Ottawa, Canada. http://www.irs.inms.nrc.ca/inms/irs/EGSnrc/EGSnrc.html

[28] Chetty I J *et al* 2007 Report of the AAPM Task Group No. 105: issues associated with clinical implementation of Monte Carlo-based photon and electron external beam treatment planning *Med. Phys.* **34** 4818–53

[29] Sempau J and Andreo P 2006 Configuration of the electron transport algorithm of PENELOPE to simulate ion chambers *Phys. Med. Biol.* **51** 3533–48

[30] Ali E S M and Rogers D W O 2008 Benchmarking EGSnrc in the kilovoltage energy range against experimental measurements of charged particle backscatter coefficients *Phys. Med. Biol.* **53** 1511

[31] Bishop H E 1965 Some electron backscattering measurements for solid targets *Proc. 4th Int. Conf. on X-ray Optics and X-ray Microanalysis* ed R Castaing *et al* (Paris: Hermann) pp 153–8

[32] Darlington E H 1975 Backscattering of 10–100 keV electrons from thick targets *J. Phys. D: Appl. Phys.* **8** 85–93

[33] Darlinski A 1981 Measurements of angular distribution of the backscattered electrons in the energy range of 5 to 30 keV *Phys. Status Solidi* a **63** 663–8

[34] Gérard P, Balladore J L, Martinez J P and Ouabbou A 1995 Experimental determination of angular-energy distributions of electrons backscattered by bulk gold and silicon samples *Scanning* **17** 377–86

[35] Kanter H 1957 On the backscattering of electrons in the energy range of 10 to 100 keV (in German) *Ann. Phys. Lpz.* **20** 144–66

[36] Kanter H 1964 Backscattering of kilovolt electrons from thin films *Br. J. Appl. Phys.* **15** 555–9

[37] Kulenkampff H and Rüttiger K 1954 Energy and angular distribution of backscattered electrons (in German) *Z. Phys.* **137** 426–34

[38] Kulenkampff H and Spyra W 1954 Energy distribution of backscattered electrons (in German) *Z. Phys.* **137** 416–25

[39] Matsukawa T, Shimizu R and Hashimoto H 1974 Measurements of the energy distribution of backscattered kilovolt electrons with a spherical retarding-field energy analyser *J. Phys. D: Appl. Phys.* **7** 695–702

[40] Wittry D B 1965 Secondary electron emission in the electron probe *Proc. 4th Int. Conf. on X-ray Optics and X-ray Microanalysis* ed R Castaing *et al* (Paris: Hermann) pp 168–80

[41] Martin J W, Yuan J, Betancourt M J, Filippone B W, Hoedl S A, Ito T M, Plaster B and Young A R 2006 New measurements and quantitative analysis of electron backscattering in the energy range of neutron β decay *Phys. Rev.* C **73** 015501

[42] Kawrakow I 2005 EGSnrc C++ class library *Technical Report* PIRS-898, National Research Council of Canada, Ottawa, Canada http://www.irs.inms.nrc.ca/EGSnrc/pirs898/

[43] Malamut C, Rogers D W O and Bielajew A F 1991 Calculation of water/air stopping-power ratios using EGS4 with explicit treatment of electron–positron differences *Med. Phys.* **18** 1222–8

[44] Kawrakow I 2002 Electron impact ionization cross sections for EGSnrc *Med. Phys.* (abstract) **29** 1230

[45] Berger M J and Hubbell J H 1987 XCOM: Photon cross sections on a personal computer *Report* NBSIR87-3597, National Institute of Standards Technology (NIST), Gaithersburg, MD 20899, USA

[46] Seltzer S M and Berger M J 1985 Bremsstrahlung spectra from electron interactions with screened atomic nuclei and orbital electrons *Nucl. Instrum. Methods Phys. Res.* B **12** 95–134

[47] Seltzer S M and Berger M J 1986 Bremsstrahlung energy spectra from electrons with kinetic energy from 1 keV to 10 GeV incident on screened nuclei and orbital electrons of neutral atoms with $Z = 1$–100 *At. Data Nucl. Data Tables* **35** 345–418

[48] Nelson W R, Hirayama H and Rogers D W O 1985 The EGS4 code system *Report* SLAC-265, Stanford Linear Accelerator Center, Stanford, CA